Integrated static and dynamic geophysical and geomechanical data for characterization of transport properties

C. Mallet, A. Isch, Gautier Laurent, C. Jodry, Mohamed Azaroual

International Journal of Rock Mechanics and Mining Sciences, in press, 2022

Integrated static and dynamic geophysical and geomechanical data for characterization of transport properties

C. Mallet[1], A. Isch[1], G. Laurent[1], C. Jodry[2], and M.Azaroual[1,3]

[1]*Universite d'Orleans, CNRS, BRGM, ISTO, UMR 7327, F-45071, Orleans, France*
[2]*ITES, Université de Strasbourg, EOST, ENGEES, CNRS, UMR 7063, Strasbourg, France*
[3]*BRGM French geological survey, Orleans, France*

Abstract The observatory of transfers in the vadose zone (OZNS-France) offers a unique support for characterizing the Beauce limestone aquifer at various spatial and temporal scales. This observatory consists of a large well associated with external boreholes dedicated to imaging, monitoring, and understanding mass and heat transfers through the vadose zone. An initial geological characterization of core samples gave valuable information on the facies encountered within the vadose zone. It is composed of highly incoherent limestones down to 7 m-depth and a massive and altered limestone rock layer from 7 to 20 m-depth. The latter presents fracturation and karstification increasing with depth. This study focuses on the hard limestone rock units and aims to quantify the level of heterogeneity through static and dynamic laboratory tests performed on core samples. Along 20 m of three boreholes, representative samples are tested through uniaxial or triaxial conditions. Elastic wave velocities are also measured. The obtained Young's modulus, compression strength, and P- and S-wave velocities highlight strong variations with depth. For example, at 14 m-depth, uniaxial maximal strength ranges from 13 to 123 MPa. In addition, at 16 m-depth, P-wave velocities are distributed from 3,650 to 5,700 m.s^{-1}. These large scatterings confirm the strong heterogeneity of the geological formations. It is interpreted in terms of a high porosity, degree of fracturation and/or initiate active karstification. The double porosity is discussed from the difference between the static and dynamic Young's modulus. Their variations are interpreted in terms of connected porosity and important crack density. This last parameter is estimated from the P- and S- wave velocities, and ranges from 0 to 0.43, with an extremum value of 1.21 around 19 m-depth. These values and variations are in good correlation with log imaging and independent permeability laboratory measurements made on the hard limestone rock units.

Keywords
Limestone aquifer
Integrated data
Double porosity
Crack Density
Permeability

Introduction

The vadose zone (VZ) is a place of critical importance considering the transfer of contaminants from the surface down to the aquifer and related to anthropic activities [*Stephens*, 1995; *Arora et al.*, 2019]. It is thus crucial to better understand, monitor and predict the mechanisms of transport within the VZ. In this context, the heterogeneity and multi-scale structure of the VZ leaves a lot of unknowns and transport properties of its facies are thus difficult to be characterized. To overcome these difficulties individual classical approaches are limited. For example, measuring permeability on the field only account for understanding the global behavior of the system [*Bogena et al.*, 2018; *Blazevic et al.*, 2020]. Coupled to field geophysical measurements, interpretations can be specified and gain in clarity [*Chalikakis et al.*, 2011; *Cassidy et al.*, 2014]. However, accuracy can still be poor due to limitation of depth of observation or resolution [*Fan et al.*, 2020]. The implementation of laboratory mesoscopic and/or microscopic investigations is a key process to explain the complexity of the VZ and better understand the transport properties. Here again, however, individual methods are limited and recent literature highlighted the importance of integrated data for transport properties characterization [*Angus et al.*, 2015; *Bjørnarå et al.*, 2016].

It has been already demonstrated that heterogeneities, as cracks and connected pores, control the transport properties, reflect the effective connectivity and quantify heat and mass transfers processes within geological formations [*Claisse et al.*, 1999; *Bernabé et al.*, 2003, 2010]. To quantify crack amount, the mechanical damage parameter introduced by *Bristow* [1960] is considered as a powerful tool. This parameter can be interpreted from elastic wave velocity variations (see the review of *Guéguen and Kachanov* [2011] and some experimental validations of *Gray et al.* [2002], *Nasseri et al.* [2007], *Mallet et al.* [2013], *Ding et al.* [2017]). However, elastic wave velocity cannot be considered alone to fully characterize transport properties since crack density does not necessarily reflect the connectivity between cracks, nor the pore network. Indeed, two crack networks can have a similar crack density but largely different permeability as already demonstrated by numerical models [*Bonneau et al.*, 2016; *Novikov et al.*, 2017] and direct microstructural observations [*Mallet et al.*, 2013].

Other experiments, as geomechanical deformations tests, are needed to comprehensively describe the behavior and dynamics of porous rocks. Indeed, it is well known that geomechanical behaviors are sensitive to the initial pore network and their connectivity. It has been well established that the initial porosity of a sample strongly affects (1) its Young's modulus [*Mazars and Pijaudier-Cabot*, 1989; *Ohtsu and Watanabe*, 2001; *Zhao et al.*, 2019], (2) its uniaxial compression strength [*Wong and Einstein*, 2009; *Peng et al.*, 2016; *Rong et al.*, 2018b], and (3) its mechanical behavior in uniaxial and

triaxial conditions [*Baud and Meredith*, 1997; *Gatelier et al.*, 2002; *Takemura and Oda*, 2005], especially when varying the pore pressure for hydraulic fracturation tests [*Reinicke et al.*, 2010; *Liu et al.*, 2014]. In addition, increasing connectivity can lead to strain localization and affect the global mechanical behavior and the *post-mortem* structure of the samples with for example, more localized failure zones [*Fortin et al.*, 2005, 2006].

Based on these considerations, the presented study uses various and complementary geophysical and geomechanical measurements to describe the porosity of the O-ZNS rock formations and try to link them to permeability measurements and lithological observations. To do so, we present here our first integrated geomechanical laboratory characterization of the O-ZNS site through elastic P- and S-wave velocities, coupled to uniaxial and triaxial tests.

In the following, section 2 presents the study site with the considered boreholes, the core samples and the experimental methodologies with the used sensors and mechanical protocols. In section 3, we present the experimental results of P- and S-wave velocities, Young's modulus, maximal strength, and Mohr-Coulomb criteria, with respect to the depth of the samples. Finally, a discussion is proposed in section 4 to interpret the observed variations in terms of double porosity based on integrated static versus dynamic data and highlight the relevance of this coupling method. They are finally compared to independent permeability laboratory measurements, direct core observations, and log imaging.

1 Methodology

1.1 O-ZNS Study site

The *Observatoire des transferts dans la Zone Non-Saturée* (Observatory of transfers in the Vadose Zone - O-ZNS) study site is a new observatory of the Critical Zone implemented since 2016 and dedicated to the characterization of the dynamics within the VZ.

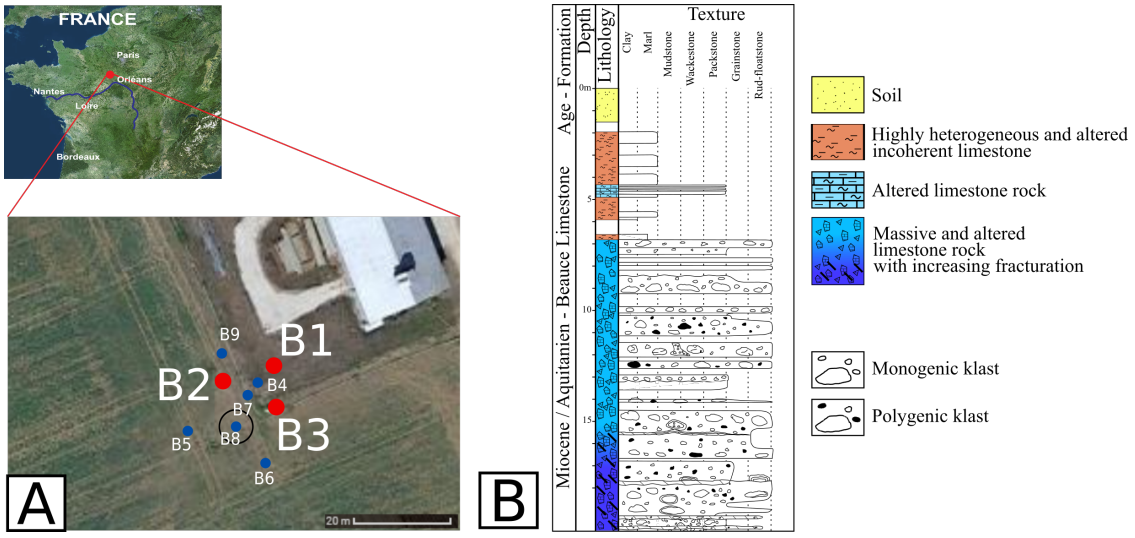

Figure 1 A: Localization of the O-ZNS study site and blow-up on the main well (black circle) with the cored boreholes. B1 to 3 (in red) are the ones drilled and cored in 2017 and mainly used for this publication. B: Interpreted geological lithology from direct core observations and borehole log imaging. Three main facies are observed. This study focuses on the hard limestone rock which extends from 7 to 20 m-depth.

O-ZNS observation site is located in the heart of the agricultural Beauce region - France (Figure 1A *Abbar et al.* [in press] - *Mallet et al.* [in press] - *Aldana et al.* [2021]). The O-ZNS aims at understanding and quantifying transfer processes thanks to a central well (20 m-depth and 4 m-diameter) surrounded by (currently) 9 boreholes dedicated to geophysical measurements and instrumented piezometers and optic fibers.

Figure 1A presents the location of the four boreholes drilled and cored in spring 2017 (B1-4). Cores used in this study are from B1 to 3 (in red). Newer boreholes (B5-9), drilled in spring 2020 are also shown for the record, but are only used here for qualitative description through direct log imaging as their analysis requires further investigations. The well localization is also shown. Its digging started in spring 2021. B8 was intentionally placed at the center of the well to preserve as much information as possible about the rocks at the well location. Therefore, B8 was destroyed during the well digging and the corresponding cores have been preserved for historical record of the O-ZNS central geology.

The first geophysical monitoring campaigns (especially with log imaging) and the direct core observations highlighted that this observatory is taking place in hard limestone rock formations affected by upstream and downstream alterations, micro-pores and cracks, macro-fracturation, and karstification [*Aldana et al.*, 2021]. A specific lithological log is proposed in Figure 1B [*Mallet et al.*, in press]. It shows the Pithiviers limestone formation that is composed of Cenozoic limestone from upper Oligocene to lower Miocene, typical of the Beauce limestones [*Guillocheau et al.*, 2000; *Wyns et al.*, 2003]:

- 0.0-1.5 m: silt loam soil typical of the Beauce region [*Ould Mohamed et al.*, 1997; *Aldana et al.*, 2021].
- 1.5-7.0 m: highly heterogeneous incoherent limestone presenting intense alteration (i.e., fractures, weathering, oxidations), powdery limestones, clay lenses, calcareous sand interbeds, and few thin massive but still altered limestone facies

- 7.0-20 m: massive and altered limestone rock presenting heterogeneous fracture density (especially deeper than 14.0 m-depth)

1.2 Samples

This work focuses on the hard limestone rock unit that is observed between 7 and 20 m-depth. The latter exhibits several kinds of lithological and structural heterogeneities, including alteration, open and connected, or not, porosity, fracturation and karstification.

The mechanical characterization developed in this study is based on the bulk property of the limestone rocks. Therefore, samples have been taken in the matrix, avoiding the macroporosity due to karstification, fractures or whatever features related to lithological interfaces. The samples are considered homogeneous at the scale of their Representative Elementary Volume (REV), but with micro-scale heterogeneities (μm to mm).

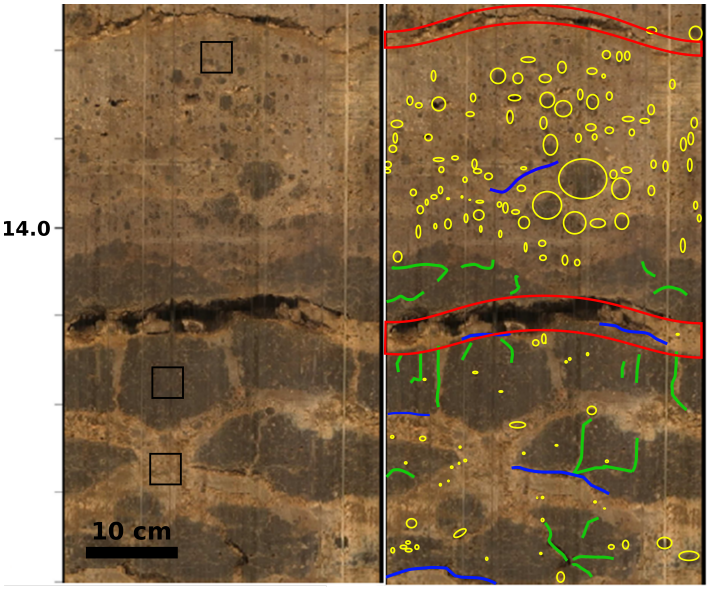

Figure 2 Highlighting of heterogeneities observed on B7 log imaging at around 14 m-depth. On the left hand side, estimation of the structural REV is proposed with black squares. On the right hand side, karsts were highlighted in red, independent spherical voids or clast in yellow, intergranular and intragranular cracks in blue and green, respectively. Vertical graduations are about 10 cm.

From direct log observation, a general REV could be estimated about 10 cm, or even more if taking into account the field scales and variations. But this is not representative of our used samples. We roughly and visually estimate our sample REV (thus avoiding macro-heterogeneities) at a few cm (as the black squares of 3×3 cm on Figure 2). Note that this virtual REV estimation is an order of magnitude that will need to be validated and confronted to scale variations. Meanwhile, this centimetric size of REV seems well to account for the microporosity and the micro-cracks, and avoid the boundary effects when considering clasts and a network of karst conduits. In these REV, the presence of heterogeneities, which are the focus of this study, have been confirmed by optical microscopy and Scanning Electron Microscopy (SEM) [*Aldana*, 2019; *Aldana et al.*, 2021]. Table 1 gives indications about the length and aperture of the observed macroscopic features observed and measured on log, core samples and through optical microscopy and SEM (Figure 2). Note that the upper size of macro-fractures and lithology changes is still unknown and will be characterized through future in-situ geophysical monitoring campaigns.

Table 1 Distribution of the macro- to micro-heterogeneities observed in log imaging of B5 to B8 and from optical microscopy and SEM. Lithological interfaces make references to the variation of geological layers that can be karstified or not.

Objects	Length		Aperture	
	min	max	min	max
Lithological interface or macro-fracturation	8 cm	–	1 cm	–
Independent void or klast	5 μm	60 mm		
Intergranular cracks	3 mm	10 cm	2 μm	6 mm
Intragranular cracks	1 mm	5 cm	1 μm	2 mm

Finally, Table A.1 in the Appendix A present the list of all samples with their depth, size, identification, and performed tests whose protocol is presented below.

1.3 Elastic wave velocity measurements

Elastic wave velocities of core samples have been measured at ambient condition on dried samples (after 24 h at 70°C). Ultrasonic piezoelectric sensors were placed directly onto the sample surface and maintained by clamps. A coupling gel was used to ensure a good contact between the sensor and the sample surface [*Couvreur and Thimus*, 1996].

A pulse of 250 V was generated and transmitted to one sensor. It was triggered into a mechanical vibration that propagates through the sample. The other sensor placed at the opposite face of the cylinder received this vibration. It transformed the vibration into an electrical signal amplified and observed on a digital oscilloscope of a sampling rate of 10 ns. Signals were recorded and arrival times were manually picked with an accuracy of 0.1 μs. Finally, by measuring the path length (sample length was from 8 to 18 cm), elastic wave velocities were obtained [*Birch*, 1960; *Yin*, 1992].

We used compressional (P) and shear (S) wave sensors to get the P- and S-wave velocities. These sensors had a resonant frequency of 50 kHz and 33 kHz for the P- and S-waves, respectively. It leads to a wavelength, λ, of 8 cm for both sensors (considering an average P- and S-wave velocities of 4,300 and 2,350 m.s^{-1} as presented below).

In order to be representative of a medium, λ needs to be higher than the REV size. Conversely, by analogy with seismic investigations, the lower limit has to be higher than $\lambda/4$ [*Sheriff and Geldart*, 1995]. This resolution corresponds to the minimal interval needed between two interfaces for them to be seen as two separate objects and not a single one, as explained by *Bailly et al.* [2019]. It leads to:

$$\frac{\lambda}{4} \leq REV \leq \lambda\,. \tag{1}$$

Thus, our sensors will be able to characterize a REV between 2 and 8 cm , which is in accordance to the REV visually estimated in the previous section.

Furthermore, we have to specify which heterogeneity size our sensors can see inside this REV. According to *Sheriff* [2002] and *Sivaji et al.* [2002], the detectable limit of a heterogeneity is between $\lambda/20$ and $\lambda/30$:

$$\frac{\lambda}{20 \sim 30} \leq heterogeneity\ size\,. \tag{2}$$

This relation implies that with our P- and S-wave sensors, we are not able to detect heterogeneities under around 2 mm. It means that all the interpretations based on velocity data and presented in this study only reflect the upper part of the micro-heterogeneities. Smaller objects, ranging from the μm to mm (Table 1) are not detected by our sensors and are not characterized by our measurements. These will be addressed during complementary ongoing investigations by using a larger branch of sensors with varying frequency up to the MHz allowing to detect smaller heterogeneities.

1.4 Uniaxial and triaxial tests

Uniaxial tests were performed on cylindrical samples of 50 mm-diameter and 100 mm-length. This size, controlled by our cell dimensions, is compatible with the structural REV size of the samples. Note that some samples derived from this size by a few millimeters, always keeping the same diameter/length ratio. Young's moduli were derived from the linear part of the stress-strain curves. In addition, maximal strength (σ_{max}) was obtained at the sample failure.

Triaxial tests were performed on cylindrical samples of 35 mm-diameter, 70 mm-length, isolated by a neoprene jacket. Here also, the size of these samples is controlled by our cell dimensions and is still in agreement with the estimated structural REV size of the samples. The confining pressure, P_C, was provided by a pump system using oil that can reach 100 MPa. In Table 2, the applied confining pressure for all tests are summarized together with the number of tested samples per core. From these conditions, Mohr-Coulomb criterium were defined in conjunction with the cohesion and friction angle properties: C'/ϕ'.

Table 2 Tested samples in triaxial conditions. For each core segment, Nb refers to the number of samples that were extracted and tested in triaxial conditions. Applied confining pressure (P_C) and maximal stress reached at failure (σ_{max}) are given for all samples.

Core id	Depth (m)	Nb	P_C (MPa)	σ_{max} (MPa)
B1-Co06	12.75 m	3	10	196.9
			20	253.2
			40	332.2
B2-Co07	11.08 m	4	10	108.0
			20	140.9
			20	220.9
			40	343.0
B3-Co06	17.47 m	4	10	166.6
			20	209.7
			40	208.5
			40	266.3

For all these mechanical uniaxial and triaxial tests, axial strains were measured using four strain gauges vertically oriented. The gauges were glued directly onto the sample surface at mid-height around the circumference. Axial strains were calculated using the average values of the four vertically oriented strain gauges. Data were recorded with a frequency of 1 Hz through a resolution of 1 μm/m thanks to a dedicated interface. The axial stress was applied by a vertical piston placed at the top of the sample. Experiments were done at a fixed displacement rate between 0.3×10^{-5} and 2×10^{-5} s^{-1} for the hardest to softest samples, respectively.

All tests were performed in dry conditions and at ambient temperature controlled by air conditioning.

2 Results

2.1 Elastic wave velocities

Figure 3 presents the axial P- and S-wave velocities with respect to the depth of origin of the sample. P-wave velocities highlight three layers. The first, above 7 m-depth with a low velocity around 1,900 m.s^{-1}. This is well correlated with the lithological description displayed on Figure 1B indicating the occurrence of the hard limestone rock below 7 m-depth. Then, between 7 and 14 m-depth, P-wave velocities do not present a specific trend and have an average value of 3,995 m.s^{-1} with a large variability of $\pm$770 m.s^{-1}. Finally, below 14 m-depth, P-wave velocities' behavior still do not display any specific trend. Yet the variability increased to $\pm$1,100 m.s^{-1} with an average value around 4,800 m.s^{-1}, higher than the upper layer average velocity.

These scattered values are not explained by uncertainties on the measurements. Indeed, considering the sensor position accuracy, the time picking accuracy, and the signal sampling, elastic wave velocities were obtained with an accuracy of $\pm$50 m.s^{-1} (as in similar studies like *Pimienta et al.* [2015a]).

S-wave velocities also highlight the same three units, although the difference is less marked between the deepest two units. Indeed, we can see that above 7 m-depth the measured S-wave velocity is low (around 1,400 m.s^{-1}). Between 7 and 14 m-depth, S-wave velocities does not present a specific trend, with variations of $\pm$470 m.s^{-1} and an average value of 2,350 m.s^{-1}. Below 14 m-depth the average value does not change significantly, but the scattering increases with the presence of two extremums (at 16.06 m and 19.66 m-depth).

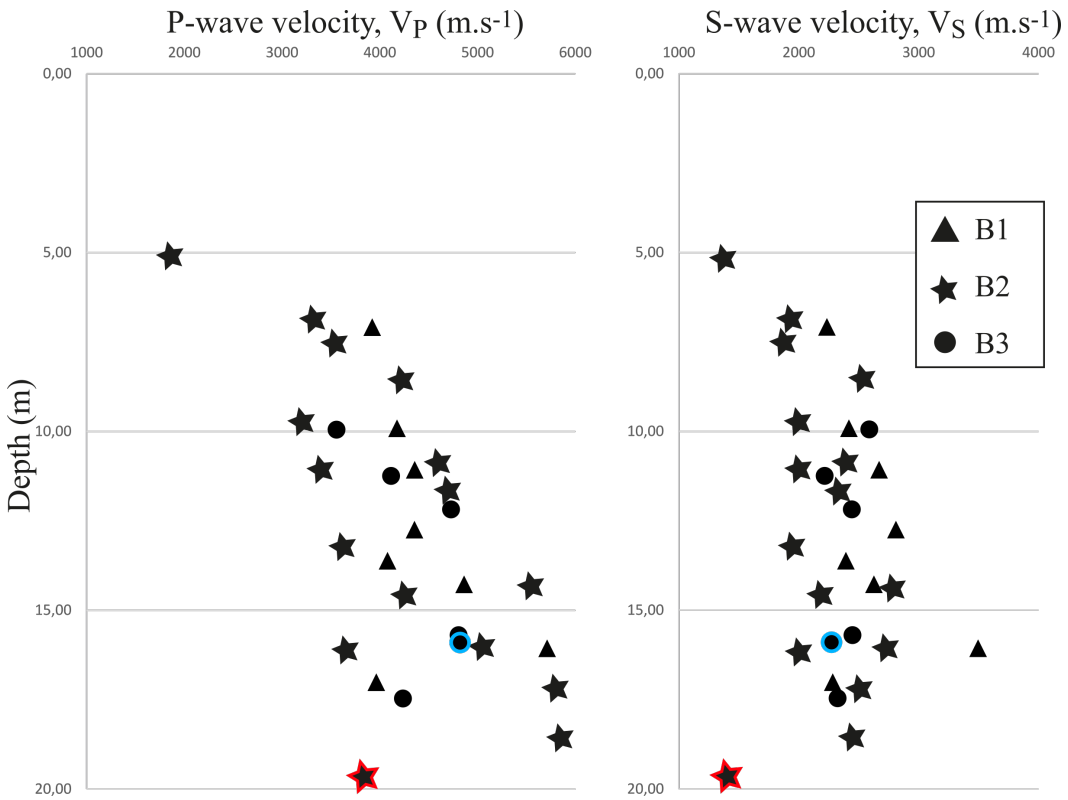

Figure 3 Elastic P- and S- wave velocities measured on core samples, plotted with respect to their depth of origin. Results from B1 to B3 are distinguished with different symbols. Points highlighted in blue and red are used for the discussion section.

2.2 Uniaxial tests and static Young's modulus

During the uniaxial tests, we observed two different behaviors: a classical elastic-brittle behavior and a strain relaxation one presenting a less marked failure. These two different behaviors are illustrated on Figure 4. This plot shows the axial strain obtained on samples B3-Co03 and B3-Co05. The obtained *post-mortem* samples can be seen in addition. On one side, B3-Co03 (12.18 m-depth) highlights a classical elastic-brittle behavior. Its failure happens at 85 MPa at a maximal strain of 0.18 % showing two large transverse fractures on the *post-mortem* sample. On the other side, B3-Co5 (15.90 m-depth) shows a relaxation strain at the beginning and a lower maximal strength (of 38.7 MPa with a maximal strain of 0.28 %)

presenting a less localized failure despite its deeper origin.

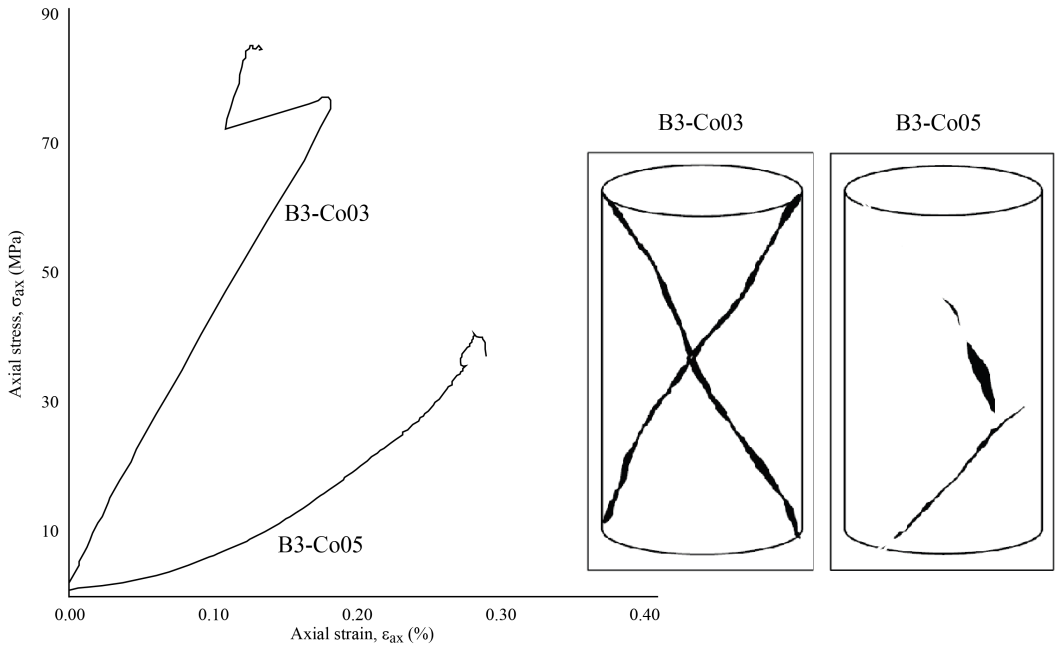

Figure 4 Strain measured on two samples submitted to uniaxial test: B3-Co03 (12.18 m-depth) and B3-Co05 (15.90 m-depth) and *post-mortem* samples.

The results obtained for all samples are specified in Table 3. They can be grouped in two main categories following the difference between B3-Co03 and B3-Co05 with some undefined classification (when samples presented an intermediate behavior between these two). Figure 5 shows the Young's modulus and maximal strength variation with depth for all tested samples.

Table 3 Summary of the uniaxial test results: Young's modulus, E, and reached maximal strength, σ_{max}. A description of the behavior is specified when clearly belonging to group 1 (elastic-brittle behavior) or 2 (relaxation behavior with lower strength).

Borehole	Core id - Depth (m)	E (GPa)	σ_{max} (MPa)	behavior
B1	Co04 – 11.20	43.4	101.9	elastic/brittle - high strength
	Co09 – 14.27	47.6	78.3	mixed behavior
	Co10 – 16.06	17.7	74.8	relaxation - low strength
	Co11 – 17.01	31.5	130.3	elastic/brittle - high strength
B2	Co04 – 8.60	24.4	77.9	mixed behavior
	Co10 – 14.39	53.0	123.1	elastic/brittle - high strength
	Co12 – 16.05	22.4	66.0	mixed behavior
	Co16 – 18.57	16.8	39.6	relaxation - low strength
B3	Co03 – 12.18	41.0	85.0	elastic/brittle - high strength
	Co05 – 15.90	17.4	38.7	relaxation - low strength

Considering these graphics and the group division, no correlation with depth appears. Indeed, no global trend was observed whatever the parameter. As for the wave velocities, a large scattering is observed with both measurements of Young's modulus and maximal strength varying from 16.8 to 53.0 GPa, and from 13.3 to 139.2 MPa, respectively.

We still remark a possible different layer with the Young's modulus. Indeed, it seems, as for the P-wave velocity, to show a rough variation around 15 m-depth. This observation could be attributed to the proposed occurrence of a unit which differed from that above from a structural point of view (depicted by the dashed line on the lithological log - Figure 1B). Indeed, above 15 m-depth, Young's modulus is quite constant around 41.0-53.0 GPa (except for one sample at 8.60 m-depth), and drop to 16.8-31.5 GPa below 15 m-depth.

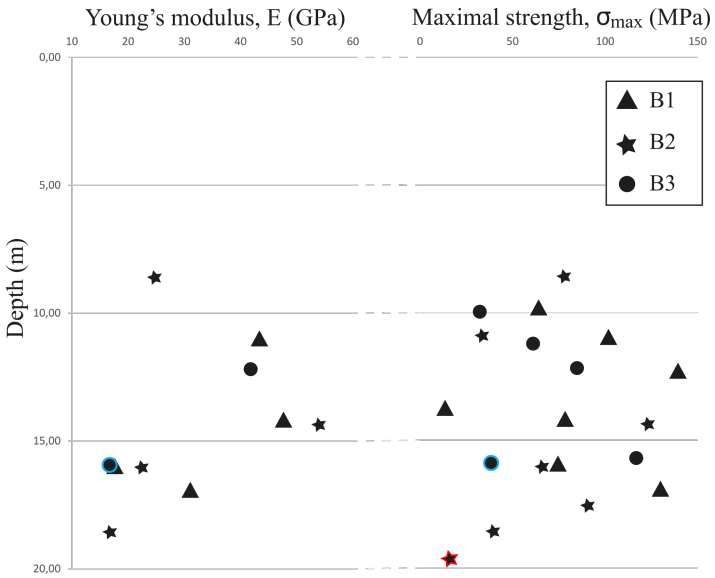

Figure 5 Young's modulus and maximal strength measured under uniaxial conditions on samples of the three boreholes (B1 to B3) from 7 to 20 m-depth. Results from B1 to B3 are differentiated with specific symbols. Points highlighted in blue and red are used for the discussion section.

2.3 Triaxial tests and Mohr-Coulomb criterium

Three cores were considered for triaxial tests (one for each borehole B1, B2 and B3). Cores have been chosen at different depths from 11 m to 17 m-depth. As seen on Table 2, 3 to 4 samples were extracted for each core. The confining pressure and reached maximal stress at failure allow us to draw Mohr circles and Mohr-Coulomb criterion (Figure 6). Depending on how the Mohr-Coulomb criterion is plotted, the obtained minimal and maximal cohesion and friction angles can be obtained and are summarized in Table 4.

Table 4 Summary of the cohesion, C', and friction angle, ϕ', obtained on the three cores depending on the possible variation of the Mohr-Coulomb criterion, based on Figure 6.

Sample	Depth	C'_{min} (MPa)	C'_{max} (MPa)	ϕ'_{min}	ϕ'_{max}
B1-Co07	12.75m	32	51	30°	41°
B2-Co08	11.08m	0	22	42°	55°
B3-Co11	17.47m	27	52	17°	32°

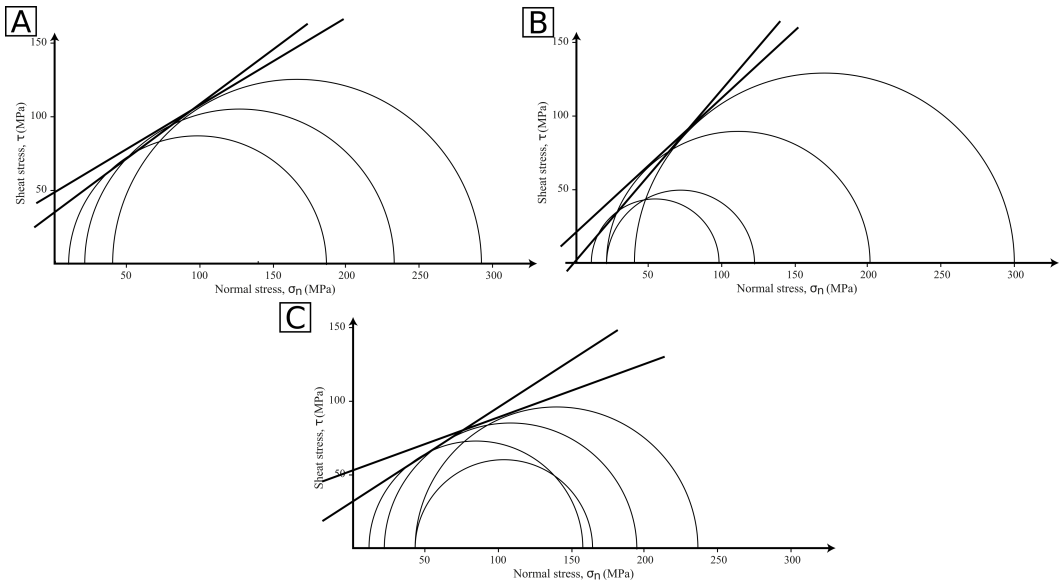

Figure 6 Mohr circles and Mohr-Coulomb criterion obtained on, A: B1-Co07 at 12.75 m-depth, B: B2-Co8 at 11.08 m-depth, C: B3-Co11 at 17.47 m-depth.

At a similar depth (with respect to the global formation) the averaged cohesion varies from 11 to 41 MPa and reveals again a high scattering (Figure 6A,B for B1-Co07 at 12.75 m-depth and B2-Co8 at 11.08 m-depth). It highlights also the high vertical and lateral heterogeneity of the mechanical properties of the geological formation of the VZ. We also observe a decrease of friction angle from 11.08 m-depth (B2-Co07) to 17.45 m-depth (B3-Co06). Unfortunately, these interpretations cannot go further. Indeed, it's worth noting that only 3 cores were tested in triaxial conditions due to the time consuming of these experiments (repeated 3 to 4 times). Further studies should focus on the tests in triaxial conditions of more samples to be more representative of the high heterogeneity and the variation with depth of the whole units of the VZ.

3 Discussion

Considering Figures 3 to 6, there is no clear trend relating the studied parameters with depth in the studied layer (7 to 20 m-depth). It is interpreted as the effect of the high vertical heterogeneity of the limestone rock matrix, which presented a global alteration but also some massive limestone banks, as described on direct core observations. Additionally, a large variability is observed between two samples located at a similar depth considering every parameter and consequently the mechanical behavior. It is interpreted in terms of significant heterogeneities and lateral variabilities of the mechanical properties of the VZ. REV has been estimated around few centimeters considering that samples have been taken without the highest heterogeneities. However, it is still possible that some intermediately higher heterogeneities have been sampled and overpass this REV. This may explain some of the important scattering observed in the presented results.

This global variability becomes even greater after 15 m-depth. Also, at this depth, Young's modulus seems to drastically decrease. We interpret this variation in terms of a much more important natural heterogeneity network below this depth. The enhancement of this heterogeneity network could be attributed to the apparition of downstream altered rock. Indeed, from this depth, the limestone alteration is increased by the variations of the water table level (which has already reached a depth of 15 m over the last few decades) and footprints of water/rock interactions [*Aldana et al.*, 2021].

The following discussion aims to quantify and describe these heterogeneities and to correlate them to the permeability of the samples and the observed lithology to assess this hypothesis.

3.1 Static vs Dynamic Young's modulus and double porosity interpretation

P- and S-wave velocities can be interpreted in terms of dynamic Young's modulus in order to be compared to the static Young's modulus. In Figure 7A, the dynamic Young's modulus can be seen in black together with the previously shown static ones in grey (from Figure 5). For the samples submitted to both uniaxial test and velocities measurements (cf. Appendix A), a red arrow shows the difference from static to dynamic values. Then, in Figure 7B, the Young's modulus difference (i.e., the difference between the high frequency value and the low frequency one, or the difference between dynamic and static values) is plotted for these specific samples.

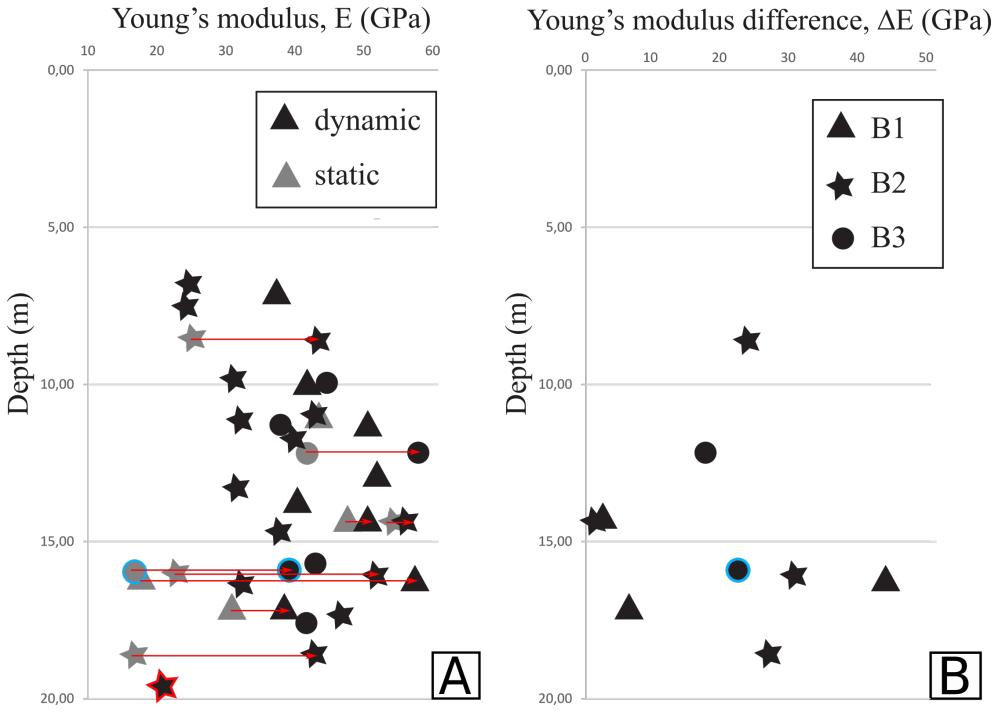

Figure 7 A: Dynamic Young's modulus calculated from P- and S-wave velocities. Corresponding static values are indicated in grey. Red arrows show the difference from static to dynamic values for samples submitted to both uniaxial tests and velocity measurements. B: Young's modulus difference for the samples submitted to both uniaxial tests and velocity measurements. All data are plotted with respect to depth. Points highlighted in blue and red are discussed in this section and correspond to the core presented in Figure 9A and B, respectively.

We clearly see that this difference is always positive with higher dynamic modulii. This is classically explained by

the stress level coming from the strain amplitude. Indeed, as Figure 4 shows, static values are measured for important strains of 10^{-3} (or even higher) while dynamic values are always measured for lower strains. It is likely then, that static measurements involve slow displacements distributed in the whole sample and impacted by all the matrix (including the porous background and defects as cracks, fractures) while dynamic measurements do not because of the lower stress level. This highlights a double porosity in our samples (with a porous background, i.e. matrix porosity, and cracks).

The amplitude of Young's modulus difference is often not negligible and reaches few tens of GPa. Yet, we observe some samples which show almost no difference between static and dynamic Young's modulus.

To try to go further in the possible interpretation of these variations of Young's modulus difference, we can hypothesize the roles of frequency and fluids. Indeed, numerical models can be found in the literature showing the strong impact of fracturation in a porous media on the frequency dependent elastic modulii [*Rubino et al.*, 2014; *Caspari et al.*, 2016; *Mallet et al.*, 2017]. These models, using double porosity principle, show through Biot's theory that Young's modulus difference between low and high frequency is enhanced with connected crack networks. Such observations have been done also in experimental works in saturated and dry conditions [*Pimienta et al.*, 2015a,b]. The phenomenon can be explained by a squirt flow process [*Pride et al.*, 2004; *Quintal et al.*, 2016]: when an elastic wave goes through a double porosity media (including pores matrix and cracks) at low frequency, the variation of pressure has the time to accommodate in the porous background, while at high frequency, the instantaneous pressure diffusion is released in the connected fractures [*Rubino et al.*, 2013].

Coupling of these two explanations (variation of stress level and frequency effects) explains that static young's modulus measured during uniaxial tests are impacted by the porous background and cracks, while dynamic ones interpreted from the P- and S-wave velocities rather are affected only by cracks. It is a coupled confirmation of O-ZNS double heterogeneity presenting strong lateral and vertical variations along the VZ column. In addition, the difference between young's modulus high and low frequency could be interpreted in terms of porosity variations.

Looking at depth variation, the Young's modulus difference starts at around 20 GPa at 8 m-depth and decreases to very low values approaching 0 GPa at around 14 m-depth. Below 15 m-depth, higher Young's modulus difference values are observed (around 40 to 50 GPa). Considering the double porosity interpretation, and remembering that we are at the relevant REV scale, the smallest difference values could correspond to strong limestone presenting a small porosity (but still potentially with cracks) probably due to a less altered layer. On the other side, the highest difference value would depict samples presenting much more independent pores (and still maybe with cracks).

In addition, this double porosity could explain the different behaviors observed during the uniaxial tests. Indeed, it confirms a different initial porosity for the two groups of samples (Table 3): in the first group, porosity is either equivalent or less important and predominated by cracks while in the second group, the more important initial porosity would be spherical pores but not cracks (or at least not connected) (see the distinction in Table 3). Indeed, the more localized failure can be a witness of the crack propagation and connectivity increase as observed by *Fortin et al.* [2006] and *Mallet et al.* [2015]. For the second group, the initial strain relaxation is classical in the literature and is attributed to the closure of pre-existing pore [*Menéndez et al.*, 1996; *Fortin et al.*, 2005].

These different initial microstructures affect and are translated by their behavior, maximal strength, Young's modulus and Young's modulus difference.

3.2 Crack density compared to the literature

The cracked part of this double porosity can be described through the crack density, a relative dimensionless mechanical parameter defined by *Bristow* [1960]. In isotropic conditions, that we consider here for sake of simplicity, it is obtained by:

$$\rho_c = \sum_{m}^{N} a_i^3 / V_T \,, \tag{3}$$

where a_i is the i^{th} crack radii over N number of cracks and V_T the total volume of the sample. From a mechanical point of view the crack density represents the volume of influence of cracks over the total volume of the sample. Thus, it defines the probability of crack interactions and their consequences on the sample macro-behavior. However, crack density does not account for the porosity neither its impact on the mechanical behavior.

Elastic wave velocities can be translated in terms of the elastic bulk, K, and shear modulus, G [*Mori and Tanaka*, 1973; *Kachanov*, 1993; *Guéguen and Kachanov*, 2011]. These modulus variations are then linked to the crack density by:

$$\frac{K_0}{K} = 1 + \frac{\rho_c}{1-2\nu_0} H \left(1 - \frac{\nu_0}{2}\right) \,, \tag{4}$$

and

$$\frac{G_0}{G} = 1 + \frac{\rho_c}{1+\nu_0} H \left(1 - \frac{\nu_0}{5}\right) \,, \tag{5}$$

where the subscript 0 denotes the non-cracked parameters ; ν_0 is the Poisson ratio ; and

$$H = \frac{16\left(1-\nu_0^2\right)}{9\left(1-\frac{\nu_0}{2}\right)} \,. \tag{6}$$

For our samples, we chose the less heterogeneous ones (those with the highest Young's modulus or velocities for example) to estimate the non-cracked modulii of K_0 and G_0 and obtain then, a relative crack density presented in Figure 8A.

Except for the extremum observed at 19.66 m-depth (ρ_c=1.21-red star), crack density ranges from 0.00 to 0.50 with an average value of 0.19. This kind of value are representative of well cracked materials. Indeed, it is similar to some observations found in the literature obtained in thermally cracked ceramics [*Ougier-Simonin et al.*, 2011; *Mallet et al.*, 2013], in natural carbonates [*Nicolas et al.*, 2016; *Bailly et al.*, 2019], in other natural crustal rocks [*Lockner*, 1993; *Browning et al.*, 2017], but also discussed and often used through numerical models [*Grechka and Kachanov*, 2006; *Novikov et al.*, 2017]. We can observe that the expected increasing variation after around 15 m-depth is not recovered here, surely hidden by the large scattering. Albeit, under this depth the average crack density increases (0.15 above 15 m-depth and 0.23 below).

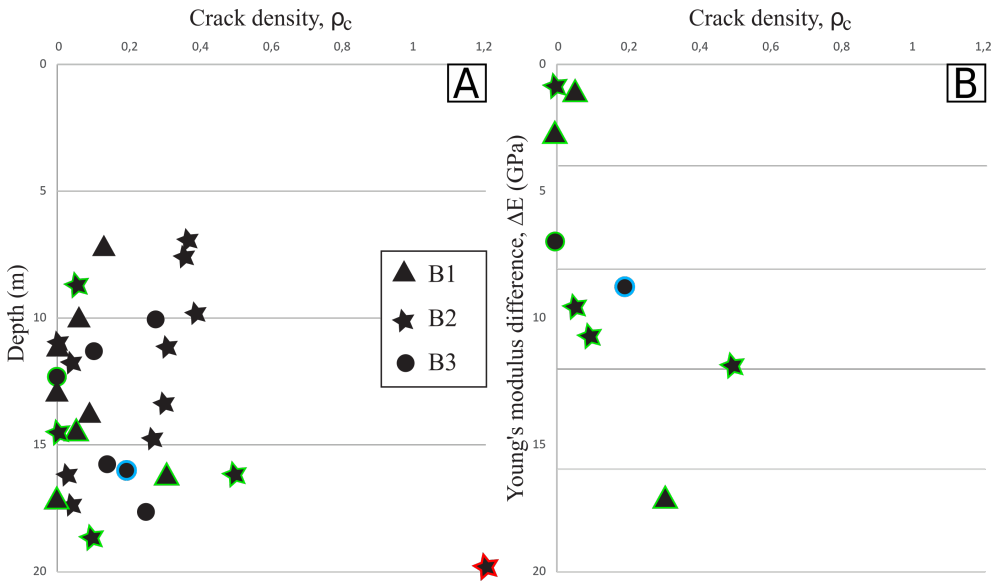

Figure 8 A: Crack density calculated from the P- and S-wave velocities of Figure 3 with respect to depth. Points highlighted in blue and red are discussed in this section and correspond to the core presented in Figure 9A and B, respectively. Points highlighted in green (and the blue one) correspond to samples for which Young's modulus is known. B: Crack density compared to Young's modulus difference for green and blue points.

The 9 samples where Young's modulus difference is known (from Figure 7B) are highlighted in green (Figure 8A and B). We can see that those with the greatest Young's modulus difference have the greatest crack density. It indicates that samples presenting an important porosity in the background also have an important crack network, while the less porous ones present a small crack amount.

Finally, two samples are discussed. They are highlighted on Figure 8A: one with a crack density corresponding to an average value of 0.19 (blue circle) and the one with the maximal crack density of 1.21 (red star).

First, the crack density of 0.19 (blue circle from B3-Co05 at 15.90 m-depth) corresponds well to intermediate velocities (blue circles on Figure 3) as expected. However, it corresponds to low Young's modulus and maximal strength (blue circles on Figure 5). It could mean that this averagely cracked sample is also composed of intermediate amount of spherical pores. This would explain also the intermediate Young's modulus difference. This observation is coherent with the group distinction of uniaxial results. This average crack density value will be compared in the following section to core observations.

Second, the extreme value observed at 19.66 m-depth, with ρ_c=1.21 is shown with a red star (B2-Co17). This value is in a good correlation with uniaxial results of Figure 5 and elastic wave velocities of Figure 3. Indeed, this naturally high crack density was coming from the low P- and S-wave velocities and explains the particularly low strength observed at this depth. We can see with Table 3 that this sample was also associated to a relaxation strain in uniaxial conditions highlighting a strong presence of initial pores.

Note that, although this value may seem mistaken because superior to 1, it is not the case. Indeed, crack density is not a simple void ratio. It is calculated with the sum of all cubed crack radius (as if we considered the sum of the spheres around all cracks). A crack density superior to 1 means that the possibility for crack to interact under mechanical test is certain. Crack densities superior to 1 have already been documented in the literature. For examples, crack densities of 1.05 or 1.90 have been measured in crustal rocks [*Zuo et al.*, 2016] or concretes [*Belayachi et al.*, 2019], when these samples were submitted to high thermal shocks. Also, under mechanical tests, crack density can exceed 1 close to the failure [*Sha et al.*, 2020]. In our case, this extreme value is not due to the failure of the sample neither a thermal solicitation. Our high value denotes a natural highly dense crack and pore networks. Such amount of natural crack density and/or double porosity has also already been observed in the literature as for example in a naturally cracked marble with a crack density of 1.04 [*Arena et al.*, 2014; *Delle Piane et al.*, 2015].

3.3 Correlation with direct observations

Figures 9A and B present some pictures of the studied core samples: (a) B1 from 10.1 m to 11.7 m-depth (from which the blue circle sample has been extracted) and (b) B2 from 19.3 m to 20.0 m-depth (from which the red star sample has been extracted). Figure 9C presents four log imaging made on boreholes drilled in spring 2020 (B5 blue borehole in Figure 1) from 11 m to 19 m-depth.

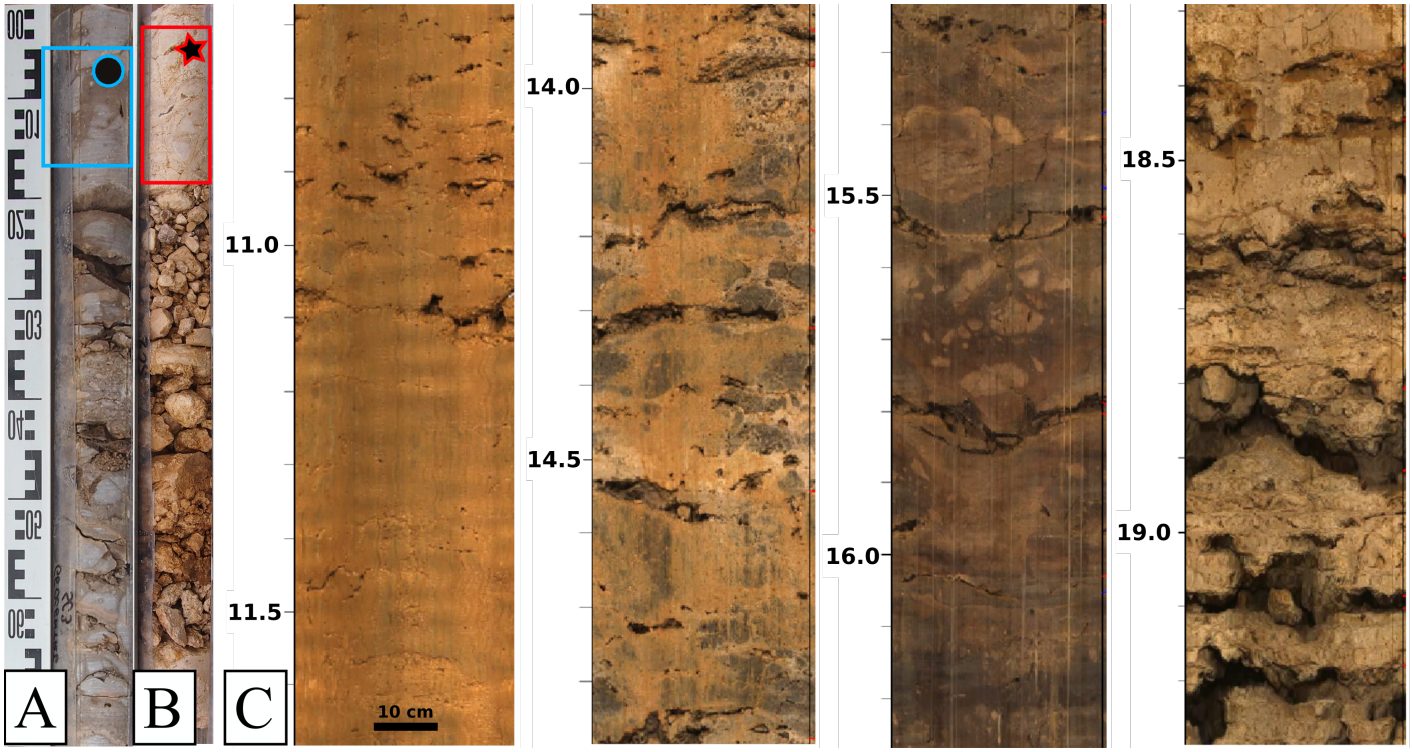

Figure 9 A: Core picture of B1 from 10.1 m to 11.7 m-depth. B: Core picture of B2 from 19.3 m to 20.0 m-depth. On these two pictures blue circle and red star highlight where the samples used in this study have been extracted. C: Log imaging made on B5 borehole of 11 cm-diameter Figure 1), at different depths with the presence of cracks becoming more and more important in the lower part.

There are three clear evidences of a good correlation between these pictures or log imaging and the estimated crack density:

- First, the sample made in the core of Figure 9A corresponds to the average crack density of 0.19 (blue circle on Figure 8). On the core direct observation we can indeed observe an existing crack network and few pores.
- Second, the core of Figure 9B coming from 19.3 to 20.0 m-depth, seems to have as much crack as solid. The samples have been extracted in the more cohesive part of the core (highlighted with the red star), but still present a huge crack network explaining the crack density higher than 1.
- Third, looking at the log imaging evolution with depth: it appears that the crack network is always present with a small to moderate density, without significant variations with respect to depth except in the last part. From 18-19 m-depth, the observed macro-crack network is much more developed. It is well correlated to the higher crack density observed at 19.66 m-depth.

3.4 Correlation with independent permeability measurement

The hydraulic properties of undisturbed cored samples from B2 have been already determined on previous studies made by *Aldana* [2019] and *Aldana et al.* [2021], using a multistep outflow method applied by using a triaxial system. The values of saturated hydraulic conductivity, K_S were obtained in m.s^{-1}. This data can be related to the intrinsic permeability, k in m^2 [*Hubbert*, 1940], which is more commonly considered in geomechanics and geophysics, by:

$$K_S = \frac{k\rho g}{\mu}, \tag{7}$$

where ρ and μ are the fluid volumic mass $[kg.m^{-3}]$ and viscosity $[Pa.s]$, respectively and g the gravity acceleration $[m.s^{-2}]$.

The results are presented in Figure 10. The lowest permeability value (8.0 10^{-18} m^2 at 7.5 m-depth, depicted by a grey star) has been obtained specifically on an intact massive limestone rock and characterize the limestone matrix. Although this value is not representative of our present study, it is still a remarkable result. Indeed, previous works showed that this weak local permeability can cause accumulation of water and lead to the occurrence of perched water tables at around 8 m-depth in the VZ profile [*Aldana et al.*, 2021] having an important impact on the transfer process within the VZ.

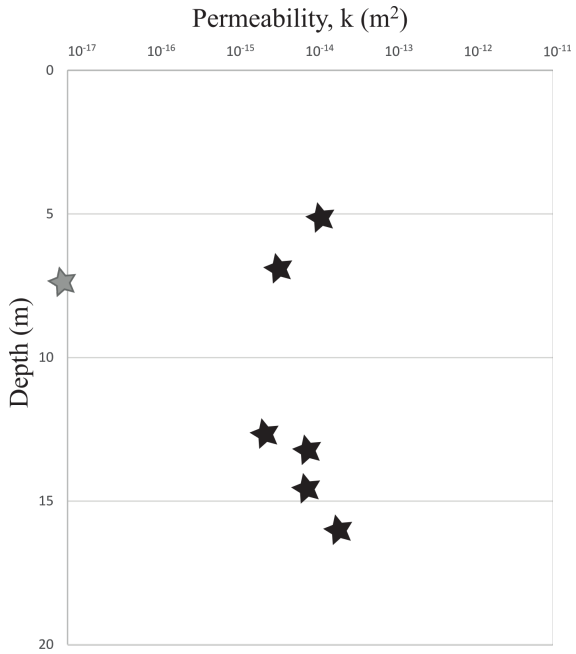

Figure 10 Permeability obtained from saturated hydraulic conductivity simulated from laboratory experiments made on six core samples from B1 and B2 (by *Aldana* [2019] and *Aldana et al.* [2021]).

The six other permeabilities are measured around 10^{-15} to 10^{-14} m^2. These values are not consistent with cracked limestone rocks [*Smith and Freeze*, 1979; *Worthington et al.*, 2016] usually starting at 10^{-13} m^2. This may be due to the fact that our samples are taken in homogeneous zone avoiding macro heterogeneities [*Aldana et al.*, 2021]. But because it is also the case for the presented geophysical and geomechanical study, our comparison can still stand.

These permeability values show, as our mechanical results, a strong variability of one order of magnitude. It seems also that permeability presents a tendency to increase with depth around 15 m-depth, which may corroborate our interpretation although the too small numbers of measurements make this point debatable.

To go further in our heterogeneity characterization, we can make a first assumption that our permeability is only due to smooth and straight cracks. Then, the cubic law could be used to estimate their corresponding average crack aperture [*Boussinesq* , 1868; *Oron and Berkowitz* , 1998]:

$$k_c = \frac{a^2}{12}\,. \tag{8}$$

The obtained crack aperture, a is about 0.2 and 0.5 μm. According to Table 1, this estimation does not fit.

This incoherence could be corrected with a further microscopic investigation to specify the finest cracks that may also contribute to the flow process. But also, we have to notice that the cubic law may be not adapted to our samples. Indeed, the first approximation drawn by the cubic law needs to be considered carefully. In the literature, its global assumption has been reexamined, especially for cracked rocks that does not have smooth and straight cracks [*Witherspoon et al.* , 1980; *Oron and Berkowitz* , 1998; *Mallet et al.*, 2017]. Considering an important crack tortuosity and roughness, a higher crack aperture would be obtained [*Wang et al.* , 2015].

We also have to be careful on the interpretation of permeability only in terms of crack aperture. Permeability is indeed, strongly affected by crack aperture, but not only. Crack length and connectivity, but also pore network (that is clearly highlighted in our samples) play a key role in transport properties both at the sample microscopic or mesoscopic scales, but also at the field scale.

4 Conclusion

This paper presents a first characterization of the micro- to meso-scale heterogeneities observed in the hard massive and altered rock units from a highly heterogeneous vadose zone of a limestone aquifer based on integrated geophysical, hydrogeological and geomechanical laboratory investigations. The measured properties (wave velocities, mechanical strength in uniaxial and triaxial conditions) highlighted no specific trend with depth but a strong lateral and vertical variability. The increases in this variability observed below 15 m-depth was attributed to an important natural damage due to heterogeneities probably sustained by mineral dissolution processes and water-rock interactions (i.e., alteration, fracturation, karstification).

The comparison between static and dynamic Young's modulus depicted a strong difference. It highlights the structure of our heterogeneities as a double porosity containing connected pores and cracks. This difference presents also a certain variability with depth indicating that the double porosity ratio is not constant over the entire VZ column.

On one side, the independent pores affect the global elastic behavior of the samples and their mechanical strength. On the other side, the crack has been quantitatively estimated through the crack density. This parameter ranges between 0.0

and 0.5, except for the deepest part of the formation (from 19 m-depth) where the crack density reaches an extreme value above 1.

These results are in good correlation with direct core lithological observation and log imaging highlighting (1) a moderate porosity and crack density between 7 and 19 m-depth, and (2) an increase of crack density in the deepest part of the VZ profile (with an extreme value at around 19 m-depth).

Finally, whether samples with high crack density or high porosity (or both), these observations are correlated with values of permeability ranging from 10^{-15} m^2 to 10^{-14} m^2. These values increase with depth, while the massive limestone rock matrix displayed much lower permeability (10^{-18} m^2). However, the comparison with permeability does not allow us to find back our microstructure estimation of crack aperture. It highlights the key role of the double porosity in transport properties and the importance to characterize all cracks (micro to macro), pores (to karsts) and connected pores. This large and complex issue represents our future investigations and ongoing work is already dedicated to Representative Elementary Volume description at different scales and characterization through various frequency measurements.

Acknowledgement
This research work was conducted within the framework of the O-ZNS project which is part of PIVOTS project. We gratefully acknowledge the financial support provided by the Région Centre-Val de Loire (ARD 2020 program and CPER 2015 -2020) and the French Ministry of Higher Education and Research (CPER 2015 -2020 and public service to BRGM). This is also co-funded by European Union with the European Regional Development Fund. Finally, this research work is co-funded by the Labex VOLTAIRE (ANR-10-LABX-100-01).
Authors are also thankful for the mechanical tests performed by C. Poinclou and T. Lando from Antea Group ; for the interpretation of sedimentology facies improved by S. Andrieu (BRGM) and B. Brigaud and K. Moreau (Geosciences Paris-Saclay - GEOPS, UMR 8148) ; and for the log imagery performed by SEMM Loging.
Data can be obtained by request to the corresponding author. In addition, they will be soon available on Zenodo.org data site with their own DOI.

Appendix A List of core samples and performed tests

Table A.1 Core samples from B1, B2 and B3 with their identification and performed tests.

Borehole	Sample	Depth (m)	Core size (cm)	V_P, V_S	σ_{max}	E	triax
B1	Co01	7.08	8	X			
	Co02	9.91	22	X	X		
	Co03	11.07	14	X			
	Co04	11.20	10		X	X	
	Co05	12.40	11		X		
	Co06	12.75	25	X			X
	Co07	13.62	11	X			
	Co08	13.82	10		X		
	Co09	14.27	18	X	X	X	
	Co10	16.06	12	X	X	X	
	Co11	17.01	18	X	X	X	
B2	Co01	5.18	15	X			
	Co02	6.87	5	X			
	Co03	7.50	10	X			
	Co04	8.60	17	X	X	X	
	Co05	9.75	10	X			
	Co06	10.90	20	X	X		
	Co07	11.08	15	X			X
	Co08	11.66	19	X			
	Co09	13.25	10	X			
	Co10	14.39	11	X	X	X	
	Co11	14.63	10	X			
	Co12	16.05	10	X	X	X	
	Co13	16.15	10	X			
	Co14	17.23	21	X			
	Co15	17.58	21		X		
	Co16	18.57	16	X	X	X	
	Co17	19.66	18	X	X		
B3	Co01	9.95	30	X	X		
	Co02	11.25	21	X	X		
	Co03	12.18	26	X	X	X	
	Co04	15.70	20	X	X		
	Co05	15.90	20	X	X	X	
	Co06	17.47	33	X			X

References

Abbar, B., A., Isch, K. Michel, H. Vincent, P., Abbasimaedeh3, M. Azaroual (2021), Fiber optic sensors for environmental monitoring: state of the art and application in heterogeneous karstic limestone vadose zone of an agricultural field - Beauce Aquifer (O-ZNS), Orleans, France. *sent to Instrumentation and Measurement Technologies for Water Cycle Management*, Springer book, chapter 2.2. *(Cited page 2)*

Aldana, C. (2019), Etude des propriétés de transfert de la zone non saturée. application aux calcaires aquitaniens de l'aquifère de beauce, Ph.D. thesis, Université d'Orléans, France. *(Cited pages 3, 11, and 12)*

Aldana, C., A. Isch, A. Bruand, M. Azaroual, and Y. Coquet (2021), Relationship between hydraulic properties and material features in a heterogeneous vadose zone of a vulnerable limestone aquifer, *Vadose Zone Journal*, *20*(4), e20127, DOI: 10.1002/vzj2.20127. *(Cited pages 2, 3, 8, 11, and 12)*

Angus, D. A., M. Dutko, T.G. Kristiansen, Q.J. Fisher, J.M. Kendall, A.F. Baird, and S. Zhao (2015), Integrated hydro-mechanical and seismic modelling of the Valhall reservoir: a case study of predicting subsidence, AVOA and microseismicity, *Geomechanics for Energy and the Environment*. *(Cited page 1)*

Arena, A., C. Delle Piane, and J. Sarout (2014), A new computational approach to cracks quantification from 2d image analysis: Application to micro-cracks description in rocks, *Computers and Geosciences*, *66*, 106–120, DOI:10.1016/j.cageo.2014.01.007. *(Cited page 10)*

Arora, B., D. Dwivedi, B. Faybishenko, R. B. Jana, and H. M. Wainwright (2019), Understanding and predicting vadose zone processes, *Reviews in Mineralogy and Geochemistry*, *85*(1), 303–328, DOI:10.2138/rmg.2019.85.10. *(Cited page 1)*

Bailly, C., J. Fortin, M. Adelinet, and Y. Hamon (2019), Upscaling of elastic properties in carbonates: A modeling approach based on a multiscale geophysical data set, *Journal of Geophysical Research: Solid Earth*, *124*(12), 13021–13038, DOI:10.1029/2019JB018391. *(Cited pages 4 and 10)*

Baud, P., and P. Meredith (1997), Damage accumulation during triaxial creep of darley dale sandstone from pore volumometry and acoustic emission, *International Journal of Rock Mechanics and Mining Sciences*, *34*(3), 24–e1, DOI:10.1016/S1365-1609(97)00060-9. *(Cited page 2)*

Belayachi, N., C. Mallet, and M. El Marzak (2019), Thermally-induced cracks and their effects on natural and industrial geomaterials, *Journal of Building Engineering*, *25*(100), 806, DOI:10.1016/j.jobe.2019.100806. *(Cited page 10)*

Bernabé, Y., U. Mok, and B. Evans (2003), Permeability-porosity relationships in rocks subjected to various evolution processes, *Pure and Applied Geophysics*, *160*(5-6), 937–960, DOI:10.1007/PL00012574. *(Cited page 1)*

Bernabé, Y., M. Li, and A. Maineult (2010), Permeability and pore connectivity: a new model based on network simulations, *Journal of Geophysical Research*, *115*(B10), DOI:10.1029/2010JB007444. *(Cited page 1)*

Birch, F. (1960), The velocity of compressional waves in rocks to 10 kilobars, part 1, *Journal of Applied Mechanics*, *65*, 1083–1102, DOI:10.1029/JZ066i007p02199. *(Cited page 4)*

Bjørnarå T.I., J.M. Nordbotten, and J. Park (2016), Vertically integrated models for coupled two-phase flow and geomechanics in porous media, *Water Resources Research* , *52*(2), 1398-1417, DOI: 10.1002/2015WR017290. *(Cited page 1)*

Blazevic, L.A., L. Bodet, S. Pasquet, N. Linde, D. Jougnot, and L. Longuevergne (2020), Time-Lapse Seismic and Electrical Monitoring of the Vadose Zone during A Controlled Infiltration Experiment at the Ploemeur Hydrological Observatory, France, *Water*, *12*(5), 1230, DOI: 10.3390/w12051230. *(Cited page 1)*

Bogena, H.R., C. Montzka, J.A. Huisman, A. Graf, M. Schmidt, M. Stockinger, and H. Vereecken (2018), The TERENO-Rur hydrological observatory: A multiscale multi-compartment research platform for the advancement of hydrological science, *Vadose Zone Journal* , *17*(1), 1-22, DOI: 10.2136/vzj2018.03.0055. *(Cited page 1)*

Bristow, J. (1960), Microcracks, and the static and dynamic elastic constants of annealed and heavily cold-worked metals, *British Journal of Applied Physics*, *11*(2), 81. *(Cited pages 1 and 9)*

Bonneau, F., Caumon, G., and Renard, P. (2016), Impact of a stochastic sequential initiation of fractures on the spatial correlations and connectivity of discrete fracture networks, *Journal of Geophysical research: Solid Earth*, *121*(8), 5641–5658, DOI: 10.1002/2015JB012451 *(Cited page 1)*

Boussinesq, J. (1868), Memoir on the influence of friction in the regular motion of fluids, *Journal of of Mathematics*, *2*. *(Cited page 12)*

Browning, J., P. G. Meredith, C. Stuart, D. Healy, S. Harland, and T. M. Mitchell (2017), Acoustic characterization of crack damage evolution in sandstone deformed under conventional and true triaxial loading, *Journal of Geophysical Research: Solid Earth*, *122*(6), 4395–4412, DOI:10.1002/2016JB013646. *(Cited page 10)*

Cassidy, R. J.-C. Comte, J. Nitsche, C. Wilson, R. Flynn and U. Ofterdinger (2014), Combining multi-scale geophysical techniques for robust hydro-structural characterisation in catchments underlain by hard rock in post-glacial regions, *Journal of hydrology* , *517*, 715-731, DOI: 10.1016/j.jhydrol.2014.06.004. *(Cited page 1)*

Caspari, E., M. Milani, J.G. Rubino, T.M. Müller, B. Quintal, and K. Holliger (2016), Numerical upscaling of frequency-dependent P-and S-wave moduli in fractured porous media, *Geophysical Prospecting* , *64*(4), 1166-1179, DOI: 10.1111/1365-2478.12393. *(Cited page 9)*

Chalikakis, K., V. Plagnes, R. Guerin, R. Valois and F. (2011), Contribution of geophysical methods to karst-system exploration: an overview, *Hydrogeology Journal* , *19*(6), 1169, DOI: 10.1007/s10040-011-0746-x. *(Cited page 1)*

Claisse, P. A., H. El-Sayad, and I. G. Shaaban (1999), Permeability and pore volume of carbonated concrete, *ACI materials Journal*, *96*(3), 378–381. *(Cited page 1)*

Couvreur, J.F., and J.F. Thimus (1996), The properties of coupling agents in improving ultrasonic transmission, *International journal of rock mechanics and mining sciences*, *33*(4), 417–424, DOI:10.1016/0148-9062(95)00074-7. *(Cited page 4)*

Delle Piane, C., A. Arena, J. Sarout, L. Esteban, and E. Cazes (2015), Micro-crack enhanced permeability in tight rocks: an experimental and microstructural study, *Tectonophysics 665*(8), 149-156, DOI:10.1016/j.tecto.2015.10.001. *(Cited page 10)*

Ding, P., B. Di, D. Wang, J. Wei, and X. Li (2017), Measurements of seismic anisotropy in synthetic rocks with controlled crack geometry and different crack densities, *Pure and Applied Geophysics*, *174*(5), 1907–1922, DOI:10.1007/s00024-017-1520-3. *(Cited page 1)*

Fan, B.,, X. Liu, Q. Zhu, G. Qin, J. Li and L. Guo (2020), Exploring the interplay between infiltration dynamics and Critical Zone structures with multiscale geophysical imaging: A review, *Geoderma* , *374*, 114431, DOI: 10.1016/j.geoderma.2020.114431. *(Cited page 1)*

Fortin, J., A. Schubnel, and Y. Guéguen (2005), Elastic wave velocities and permeability evolution during compaction of bleurswiller sandstone, *International Journal of Rock Mechanics and Mining Sciences*, *42*(7), 873–889, DOI:10.1016/j.ijrmms.2005.05.002. *(Cited pages 2 and 9)*

Fortin, J., S. Stanchits, G. Dresen, and Y. Guéguen (2006), Acoustic emission and velocities associated with the formation of compaction bands in sandstone, *Journal of Geophysical Research*, *111*(B10), 854, DOI:10.1029/2005JB003. *(Cited pages 2 and 9)*

Gatelier, N., F. Pellet, and B. Loret (2002), Mechanical damage of an anisotropic porous rock in cyclic triaxial tests, *International Journal of Rock Mechanics and Mining Sciences*, *39*(3), 335–354, DOI:10.1016/S1365-1609(02)00029-1. *(Cited page 2)*

Gray, D., G. Roberts, and K. Head (2002), Recent advances in determination of fracture strike and crack density from P-wave seismic data, *The Leading Edge*, *21*(3), 280–285, DOI:10.1190/1.1463778. *(Cited page 1)*

Grechka, V., and M. Kachanov (2006), Effective elasticity of rocks with closely spaced and intersecting cracks, *Geophysics*, *71*(3), D85–D91, DOI:10.1190/1.2197489. *(Cited page 10)*

Guéguen, Y., and M. Kachanov (2011), Effective elastic properties of cracked rocks - an overview, in, mechanics of crustal rocks, *CISM Courses and Lectures*, *533*, 73–125, DOI:10.1007/978-3-7091-0939-7_3. *(Cited pages 1 and 9)*

Guillocheau, F., Robin, C., Allemand, P., Bourquin, S., Brault, N., Dromart, G., Friedenberg, R., Garcia, J.-P., Gaulier, J.-M., Gaumet, F., Grosdoy, B.,

Hanot, F., Le Strat, P., Mettraux, M., Nalpas, T., Prijac, C., Rigoltet, C., Serrano, O., and Grandjean, G. (2000), Meso-Cenozoic geodynamic evolution of the Paris Basin: 3D stratigraphic constraints *Geodinamica Acta*, *13*(4), 189–245, DOI: 10.1080/09853111.2000.111053 *(Cited page 2)*

Hubbert, M. K. (1940), The theory of ground-water motion, *The Journal of Geology*, *48*(8, Part 1), 785–944, DOI:10.1086/624930. *(Cited page 11)*

Kachanov, M. (1993), Elastic solids with many cracks and related problems, *Advances in applied mechanics*, *30*, 259–445, DOI:10.1016/S0065-2156(08)70176-5. *(Cited page 9)*

Liu, T., P. Cao, and H. Lin (2014), Damage and fracture evolution of hydraulic fracturing in compression-shear rock cracks, *Theoretical and Applied Fracture Mechanics*, *74*, 55–63, DOI:10.1016/j.tafmec.2014.06.013. *(Cited page 2)*

Lockner, D. (1993), Room temperature creep in saturated granite, *Journal of Geophysical Research*, *98*(B1), 475–487, DOI: 10.1029/92JB01,828. *(Cited page 10)*

Mallet, C., J. Fortin, Y. Guéguen, and F. Bouyer (2013), Effective elastic properties of cracked solids: an experimental investigation, *International Journal of Fracture*, *182*(2), DOI: 10.1007/s10,704–013–9855–y. *(Cited pages 1 and 10)*

Mallet, C., J. Fortin, Y. Guéguen, and F. Bouyer (2015), Brittle creep and subcritical crack propagation in glass submitted to triaxial conditions, *Journal of Geophysical Research*, *120*(2), 879–893, DOI:10.1002/2014JB011231. *(Cited page 9)*

Mallet, C., B. Quintal, E. Caspari, and K. Holliger (2017), Frequency-dependent attenuation in water-saturated cracked glass based on creep tests, *Geophysics*, *82*(3), 89-96, DOI: 10.1190/GEO2016-0142.1. *(Cited pages 9 and 12)*

Mallet, C., C. Jordy, A. Isch, G. Laurent, J. Deparis and M. Azaroual (under review), Multi-geophysical field measurements to characterize lithological and hydraulic properties of a multi-scale karstic and fractured limestone vadose zone: Beauce aquifer (O-ZNS), *sent to Instrumentation and Measurement Technologies for Water Cycle Management*, Springer book, chapter 4.8. *(Cited page 2)*

Mazars, J., and G. Pijaudier-Cabot (1989), Continuum damage theory: application to concrete, *Journal of engineering mechanics*, *115*(2), 345–365, DOI:10.1061/(ASCE)0733-9399(1989)115:2(345). *(Cited page 1)*

Menéndez, B., W. Zhu, and T.-F. Wong (1996), Micromechanics of brittle faulting and cataclastic flow in berea sandstone, *Journal of structural geology*, *18*(1), 1–16, DOI:10.1016/0191-8141(95)00076-P. *(Cited page 9)*

Mori, T., and K. Tanaka (1973), Average stress in matrix and average elastic energy of materials with misfitting inclusions, *Acta metallurgica*, *21*(5), 571-574, DOI:10.1016/0001-6160(73)90064-3. *(Cited page 9)*

Nasseri, M., A. Schubnel, and R. Young (2007), Coupled evolutions of fracture toughness and elastic wave velocities at high crack density in thermally treated westerly granite, *International Journal of Rock Mechanics and Mining Sciences*, *44*(4), 601–616, DOI:10.1016/j.ijrmms.2006.09.008. *(Cited page 1)*

Nicolas, A., J. Fortin, J. Regnet, A. Dimanov, and Y. Guéguen (2016), Brittle and semi-brittle behaviours of a carbonate rock: influence of water and temperature, *Geophysical Journal International*, *206*(1), 438–456, DOI:10.1093/gji/ggw154. *(Cited page 10)*

Novikov, M., E. Caspari, K. Holliger, B. Quintal, V. Lisitsa, J. G. Rubino, and K. Holliger (2017), Numerical study of fracture connectivity response in seismic wavefields, in *SEG Technical Program Expanded Abstracts 2017*, pp. 3786–3790, Society of Exploration Geophysicists. *(Cited pages 1 and 10)*

Ohtsu, M., and H. Watanabe (2001), Quantitative damage estimation of concrete by acoustic emission, *Construction and Building Materials*, *15*(5-6), 217–224, DOI:10.1016/S0950-0618(00)00071-4. *(Cited page 1)*

Oron, A. P. and Berkowitz, B. (1998) Flow in rock fractures: The local cubic law assumption reexamined, *Water Resources Research*, *34*, 2811–2825, DOI:10.1029/98WR02285. *(Cited page 12)*

Ougier-Simonin, A., Y. Guéguen, J. Fortin, A. Schubnel, and F. Bouyer (2011), Permeability and elastic properties of cracked glass under pressure, *Journal of Geophysical Research*, *116*, B07,203, DOI:10.1029/2010JB008,077. *(Cited page 10)*

Ould Mohamed, S., A. Bruand, L. Bruckler, P. Bertuzzi, B. Guillet, and L. Raison (1997), Estimating Long-Term Drainage at a Regional Scale Using a Deterministic Model, *Soil Science Society of America Journal*, *61*(5), 1473-1482, DOI:10.2136/sssaj1997.03615995006100050027x. *(Cited page 2)*

Peng, J., G. Rong, M. Cai, M.-D. Yao, and C.-B. Zhou (2016), Physical and mechanical behaviors of a thermal-damaged coarse marble under uniaxial compression, *Engineering Geology*, *200*, 88–93, DOI:10.1016/j.enggeo.2015.12.011. *(Cited page 1)*

Pimienta, L., J. Fortin, and Y. Guéguen (2015a), Bulk modulus dispersion and attenuation in sandstones, *Geophysics*, *80*(2), D111–D127, DOI: 10.1190/geo2014–0335.1. *(Cited pages 5 and 9)*

Pimienta, L., J. Fortin, and Y. Guéguen (2015b), Experimental study of Young's modulus dispersion and attenuation in fully saturated sandstones, *Geophysics*, *80*(5), L57-72, DOI: 10.1190/geo2014-0532.1. *(Cited page 9)*

Pride, S. R., J.G. Berryman, and J.M. Harris (2004), Seismic attenuation due to wave-induced flow, *Journal of Geophysical Research: Solid Earth* , *109*(B1), DOI: 10.1029/2003JB002639. *(Cited page 9)*

Quintal, B., J.G. Rubino, E. Caspari, and K. Holliger (2016), A simple hydromechanical approach for simulating squirt-type flow, *Geophysics*, *81*(4), D335-344, DOI: 10.1190/geo2015-0383.1. *(Cited page 9)*

Reinicke, A., E. Rybacki, S. Stanchits, E. Huenges, and G. Dresen (2010), Hydraulic fracturing stimulation techniques and formation damage mechanisms: Implications from laboratory testing of tight sandstone–proppant systems, *Geochemistry*, *70*, 107–117, DOI:10.1016/j.chemer.2010.05.016. *(Cited page 2)*

Rong, G., J. Peng, M. Yao, Q. Jiang, and L. N. Y. Wong (2018), Effects of specimen size and thermal-damage on physical and mechanical behavior of a fine-grained marble, *Engineering Geology*, *232*, 46–55, DOI:10.1016/j.enggeo.2017.11.011. *(Cited page 1)*

Rubino, J. G., L. Guarracino, T.M. Müller, and K. Holliger (2013), Do seismic waves sense fracture connectivity?, *Geophysical Research Letters*, *40* (4), 692-696, DOI: 10.1002/grl.50127. *(Cited page 9)*

Rubino, J. G., T.M. Müller, L. Guarracino, M. Milani, and K. Holliger (2014), Seismoacoustic signatures of fracture connectivity, *Journal of Geophysical Research: Solid Earth* , *119* (3), 2252-2271, DOI: 10.1002/2013JB010567. *(Cited page 9)*

Sha, S., G. Rong, Z. Chen, B. Li, and Z. Zhang (2020), Experimental evaluation of physical and mechanical properties of geothermal reservoir rock after different cooling treatments, *Rock Mechanics and Rock Engineering*, *53*(11), 4967-4991, DOI:10.1007/s00603-020-02200-5. *(Cited page 10)*

Sheriff, R., and L. Geldart (1995), Exploration seismology, *Cambridge university press*. *(Cited page 4)*

Sheriff, R. E. (2002), Encyclopedic dictionary of applied geophysics, *Society of exploration geophysicists*, DOI:10.1190/1.9781560802969. *(Cited page 4)*

Sivaji, C., O. Nishizawa, G. Kitagawa, and Y. Fukushima (2002), A physical-model study of the statistics of seismic waveform fluctuations in random heterogeneous media, *Geophysical Journal International*, *148*(3), 575–595, DOI:10.1046/j.1365-246x.2002.01606.x. *(Cited page 4)*

Smith, L., and R.A. Freeze (1979), Stochastic analysis of steady state groundwater flow in a bounded domain: 2. Two dimensional simulations, *Water Resources Research*, *15*(6), 1543-1559, DOI:10.1029/WR015i006p01543. *(Cited page 12)*

Stephens, D. B. (1995), Vadose zone hydrology, *CRC press*. *(Cited page 1)*

Takemura, T., and M. Oda (2005), Changes in crack density and wave velocity in association with crack growth in triaxial tests of inada granite, *Journal of Geophysical Research: Solid Earth*, *110*(B5), DOI:10.1029/2004JB003395. *(Cited page 2)*

Wang, L., Cardenas, M. B., Slottke, D. T., Ketcham, R. A. and Sharp, J. M. (2015), Modification of the local cubic law of fracture flow for weak inertia, tortuosity, and roughness, *Water Resources Research*, *51*, 2064–2080, DOI:10.1002/2014WR015815. *(Cited page 12)*

Witherspoon, P. A., Wang, J. S. Y., Iwai, K., and Gale, J. E. (1980), Validity of cubic law for fluid flow in a deformable rock fracture, *Water Resources Research*, *16*, 1016–1024, DOI:10.1029/WR016i006p01016. *(Cited page 12)*

Wong, L., and H. Einstein (2009), Systematic evaluation of cracking behavior in specimens containing single flaws under uniaxial compression, *International Journal of Rock Mechanics and Mining Sciences*, *46*(2), 239–249, DOI:10.1016/j.ijrmms.2008.03.006. *(Cited page 1)*

Worthington, S.R., Davies, G.J., and Alexander Jr, E.C. (2016), Enhancement of bedrock permeability by weathering, *Earth-Science Reviews*, *1606*, 188–202, DOI:10.1016/j.earscirev.2016.07.002. *(Cited page 12)*

Wyns, R., Quesnel, F., Simon-Coincon, R., Guillocheau, F., and Lacquement, F. (2003), Major weathering in France related to lithospheric deformation, *Géologie de la France*, *1*, 79–87 *(Cited page 2)*

Yin, H. (1992), Acoustic velocity and attenuation of rocks: isotropy, intrinsic anisotropy, and stress-induced anisotropy, Ph.D. thesis, University Microfilms International, Ann Arbor, Mich. *(Cited page 4)*

Zhao, X., H. Xu, Z. Zhao, Z. Guo, M. Cai, and J. Wang (2019), Thermal conductivity of thermally damaged beishan granite under uniaxial compression, *International Journal of Rock Mechanics and Mining Sciences*, *115*, 121–136, DOI:10.1016/j.ijrmms.2019.01.014. *(Cited page 1)*

Zuo, J.-P., X.-S. Wang, D.-Q. Mao, C.-L. Wang, and G.-h. Jiang (2016), T–m coupled effects on cracking behaviors and reliability analysis of double-notched crustal rocks, *Engineering Fracture Mechanics*, *158*, 106–115, DOI:10.1016/j.engfracmech.2015.11.001. *(Cited page 10)*